A multiscale approach to diffraction tomography of complex three-dimensional objects

F. Simonetti, L. Huang, and N. Duric

Related Articles

A multi-view time-domain non-contact diffuse optical tomography scanner with dual wavelength detection for intrinsic and fluorescence small animal imaging
Rev. Sci. Instrum. 83, 063703 (2012)

A gantry-based tri-modality system for bioluminescence tomography
Rev. Sci. Instrum. 83, 043708 (2012)

Electrical capacitance tomography using an accelerated proximal gradient algorithm
Rev. Sci. Instrum. 83, 043704 (2012)

Superficial magnetic imaging by an xy-scanner of three magnetoresistive channels
Rev. Sci. Instrum. 83, 033705 (2012)

Determining the equation of state of amorphous solids at high pressure using optical microscopy
Rev. Sci. Instrum. 83, 033702 (2012)
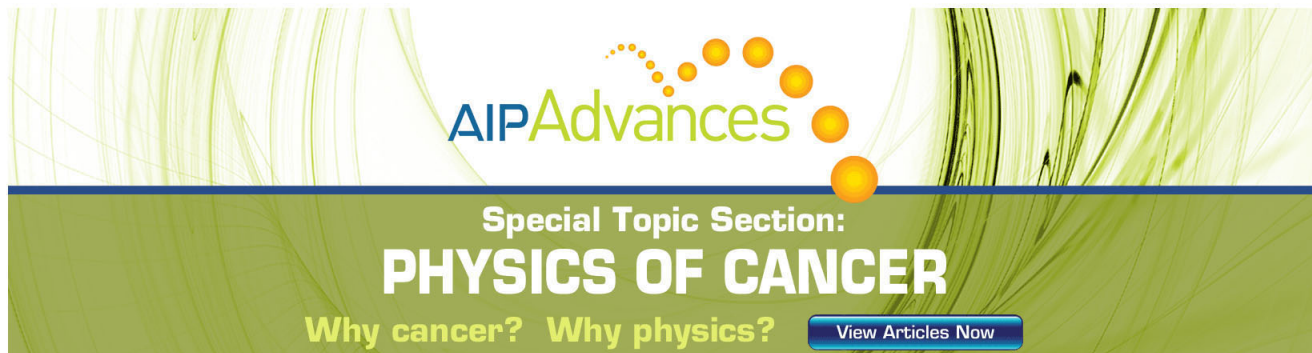
Additional information on Appl. Phys. Lett.

Journal Homepage: http://apl.aip.org/
Journal Information: http://apl.aip.org/about/about_the_journal
Top downloads: http://apl.aip.org/features/most_downloaded
Information for Authors: http://apl.aip.org/authors

A multiscale approach to diffraction tomography of complex three-dimensional objects

F. Simonetti,[1,a)] L. Huang,[2] and N. Duric[3]

[1]*Department of Mechanical Engineering, Imperial College, London SW7 2AZ, United Kingdom*
[2]*MS D443, Los Alamos National Laboratory, Los Alamos, New Mexico 87545, USA*
[3]*Karmanos Cancer Institute, Wayne State University, 4100 John R, Detroit, Michigan 48201, USA*

Tomography of complex three-dimensional objects with diffractive waves remains an open challenge due to the large number of scattering measurements required to obtain a stable solution to the inverse problem of reconstructing an image of the object from a set of independent scattering experiments. Here, this problem is addressed with a multiscale approach that is demonstrated experimentally using ultrasonic waves and which leads to high resolution images comparable to x-ray computerized tomography but without the limitations associated with ionizing radiation. © 2009 American Institute of Physics. [DOI: 10.1063/1.3204021]

X-ray computerized tomography (CT) has provided a unique window into the anatomy of the human body since the invention of the CT scanner by Hounsfield in 1972. However, the presence of ionizing radiation still limits its use to relatively low resolution applications. In fact, the higher the resolution the greater the number of x-ray projections required and the higher the radiation dose for patients. Thus, for instance, CT cannot be used for breast cancer screening. In contrast, ultrasound is devoid of risk and the possibility of developing it into a safe tomography modality has attracted much interest since early 1970s.[1]

There are two fundamental aspects that distinguish how ultrasound and x-ray radiation interact with biological tissue. First, the absorption of x-ray depends on mass density according to Beer-Lambert's law; therefore, the absorption contrast observed in a CT image can be related to density variations across an object. In clinical applications, this leads to a clear separation between soft tissue and bones while the contrast within soft tissue might be not sufficient. Therefore, techniques that exploit the phase shift of x rays rather than their absorption are being developed.[2] In contrast, ultrasound is also sensitive to the elastic moduli of a solid or the compressibility of a liquid, and the amplitude and phase of the scattered field can be readily measured without the need for interferometric techniques. Second, the interaction of x-ray with biological tissue can be described by ray theory whereas, diffraction effects are not negligible in the case of ultrasound due to the wavelength approaching the scale of tissue structures (typically 0.1–1 mm).

The ray approximation simplifies the inverse problem of reconstructing the absorption coefficient map from the measurements, as the x-ray intensity measured at a particular detector depends on the line integral from the source to the receiver of the absorption coefficient. In contrast, the encoding of information in ultrasonic measurements is more complicated as it is no longer possible to confine the region of interaction to a ray. To unravel this information, the so-called inverse scattering problem has to be solved. Although the solution (image) exists and is unique, provided that all the independent scattering measurements can be collected, the problem is ill-posed in the sense of Hadamard as the solution

is unstable, i.e., the reconstruction is not a continuous function of the input (measurements). The instability is triggered by the presence of measurement noise and is amplified when the set of independent scattering measurements is incomplete. For an object with characteristic radius R_0, the maximum order of the scattered partial waves leads to a number of independent measurements which is $N \sim (4\pi R_0/\lambda)^2$ in two dimensions (2D) and $N \sim (4\pi R_0/\lambda)^4$ in three dimensions (3D), where λ is the wavelength.[3] These measurements can be performed with an array consisting of $\sqrt{N}$ transducers deployed around the object. Each transducer illuminates the object and all the transducers, including the transmitter, measure the scattered field, according to the diagram shown in Fig. 1(a), thus leading to N measurements in total. However, while this is feasible in 2D for a realistic object with $R_0 \sim 50\lambda$ (in breast imaging with ultrasound at 1.5 MHz $\lambda = 1$ mm) using toroidal arrays,[4] the 3D case is beyond the capabilities of current technology due to the vast number of transducers required. Therefore, current experimental studies of ultrasound tomography have made use of the ray approximation that allows a slice of the object in the plane of a toroidal array to be decoupled from the rest of the object. This leads to what is known as ultrasonic computed tomography[1] or travel-time tomography (TTT).[5] However, the ray approximation is known to cause resolution degradation and image artifacts due to its inability to account for
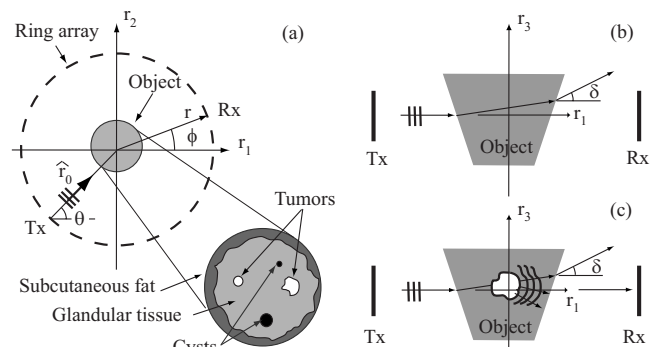

FIG. 1. (a) A circular aperture consists of an array of sensors used to probe a complex 3D object shown in the cartoon. (b) Cross section of the array with an axysimmetric object showing beam divergence. (c) Forward scattering produced by an internal mass.

a)Electronic mail: f.simonetti@imperial.ac.uk.
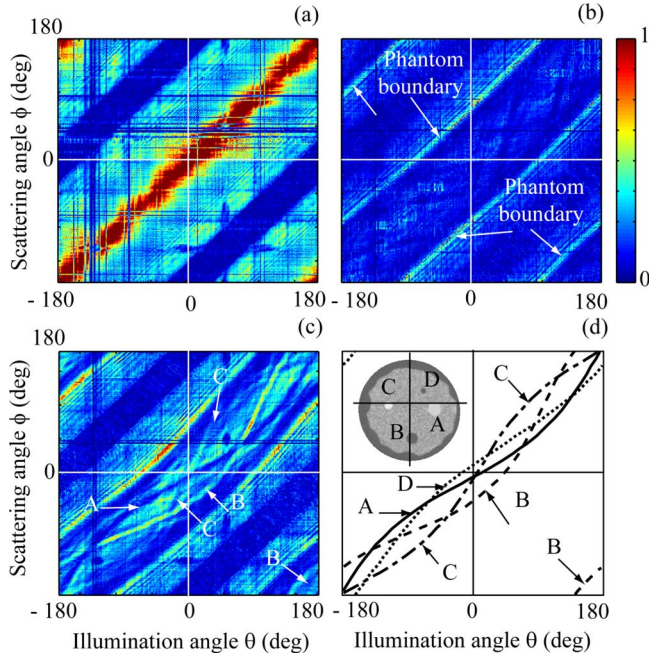
95, 061904-1

FIG. 2. (Color online) Scattering measurements performed with the array (color scale is the same in a.u.). (a) No phantom is immersed in the water background. (b) The plane of the aperture intersects the phantom but not the inclusions. (c) The aperture intersects the inclusions. (d) Transmit-receive pairs mostly affected by the inclusions.

diffraction and ultrasound tomography has not yet found clinical or industrial applications.

This letter introduces a multiscale approach aimed at high resolution imaging of targeted structures within a complex 3D object probed with a toroidal array that forms a circular aperture. The main idea is that structures with a characteristic size comparable to λ and contained in the plane of the aperture can be separated from the global 3D structure of the object using wave refraction and diffraction. We assume that scattering within the fine structures can be described by weak scattering models such as the Born approximation. Here, we consider ultrasound; however, the approach applies to other mechanical and electromagnetic waves.

Let us consider the case of a homogeneous axisymmetric object with the cross section shown in Fig. 1(b) and immersed in a homogeneous background. Assuming that λ is much smaller than the characteristic size of the object, ray theory predicts that the refracted wave emerging from the object diverges from the original propagation direction [Fig. 1(b)] in a similar fashion to the deflection experienced by a light beam passing through a prism.[6] As a result, the sensors (R_x) opposite to the source do not detect the beam. The ultrasonic field ψ, can be described by the inhomogeneous Helmholtz equation, $(\nabla^2 + k^2)\psi(\mathbf{r}, \omega) = -k^2 O(\mathbf{r}, \omega)\psi(\mathbf{r}, \omega)$,[7] where k is the background wavenumber ($2\pi/\lambda$) and ω is the angular frequency. The object is described by the so-called object function, $O(\mathbf{r}, \omega)$, of support D corresponding to the volume occupied by the object. Here, it is assumed that density variations across the object and material absorption can be neglected. Therefore, $O(\mathbf{r}) = [c_0/c(\mathbf{r}, \omega)]^2 - 1$, where c_0 is the speed of sound of the background and c the local speed of sound inside the object. The speed of sound and the compressibility, χ, are related via $c^{-1} = \sqrt{\rho\chi}$ where ρ is the density. The objective of ultrasound tomography is to reconstruct the object function from the scattering measurements.

This can provide useful diagnostic information since, for instance, it is know that a cancer mass tends to have higher Young's modulus than healthy tissue.[8] Applications of the Green's theorem and Sommerfeld condition to the Helmholtz equation lead to the Lippman–Schwinger equation

$$\psi(\mathbf{r}, k\hat{\mathbf{r}}_0) = \psi_0(\mathbf{r}, k\hat{\mathbf{r}}_0) - \int_D d^3 r' G(\mathbf{r}, \mathbf{r}') O(\mathbf{r}') \psi(\mathbf{r}', k\hat{\mathbf{r}}_0), \quad (1)$$

where $\psi_0(\mathbf{r}, k\hat{\mathbf{r}}_0) = \exp(ik\hat{\mathbf{r}}_0 \cdot \mathbf{r})$ is an incident plane wave that illuminates the object from direction $\hat{\mathbf{r}}_0$ and $G(\mathbf{r}, \mathbf{r}')$ is the free space Green function. Now let us consider the case in which inclusions with speed of sound $c + \Delta c$ and characteristic size comparable to λ are contained inside the object as shown in Fig. 1(c). The contrast Δc is a function of space and vanishes outside the inclusions. Let O^t be the new object function and $O^p = O^t - O$. For weak inclusions with $\Delta c/c \ll 1$ and to the first order approximation, $O^p \approx -2c_0^2/c^3 \Delta c$ which is proportional to the sound speed contrast of the inclusions. With inclusions, Eq. (1) becomes

$$\psi^p = \psi_0 - \int_D d^3 r' G[O + O^p]\psi^p, \quad (2)$$

where ψ^p is the new total field and the arguments of the functions have been dropped for brevity. The total field inside the object can be decomposed into the total field observed without the inclusion and a weaker field due to the inclusion, ψ', i.e., $\psi^p = \psi + \psi'$ with $\psi' \ll \psi$. By subtracting Eq. (1) from Eq. (2) and using the definition of ψ', ψ^p becomes

$$\psi^p = \psi - \int_D d^3 r' G[O + O^p]\psi' - \int_D d^3 r' G O^p \psi. \quad (3)$$

The field emerging from the object contains three main components. The field ψ is the dominant deflected wave that would be observed in the absence of the inclusion. The two additional weaker fields described by the integral terms depend on the properties of the inclusions O^p. However, since $\psi' \ll \psi$ the first integral on the RHS of Eq. (3) can be neglected. It is now observed that the integral of Eq. (3) in the direction perpendicular to the plane of the aperture, $\hat{\mathbf{r}}_\perp$, over the interval $[-\Delta, \Delta]$ with $\Delta > \lambda$ is

$$\int_{-\Delta}^{\Delta} dr_3' \psi^p = -\int_{-\Delta}^{\Delta} dr_3' \int_D d^3 r' G O^p \psi, \quad (4)$$

where the contribution from ψ becomes negligible thanks to the beam deflection phenomenon discussed before. The LHS in Eq. (4) represents the measurement from an array element that has a small ($<\lambda$) width in the circumferential direction and a 2Δ aperture along $\hat{\mathbf{r}}_\perp$.

The object O^p can be reconstructed by inverting Eq. (4). For this purpose the far-field expression $G(\mathbf{r}, \mathbf{r}') = -\exp(ikr - ik\hat{\mathbf{r}} \cdot \mathbf{r}')/4\pi r$ and the Born approximation[6] $\psi \approx \exp(ik\hat{\mathbf{r}}_0 \cdot \mathbf{r})$ are used in Eq. (4) to obtain

$$\int_{-\Delta}^{\Delta} dr_3' \psi^p = \frac{\exp(ikr)}{4\pi r} \int_{-\Delta}^{\Delta} dr_3' \tilde{O}_{3D}^p \{k[\hat{\mathbf{r}}(r_3') - \hat{\mathbf{r}}_0]\}, \quad (5)$$

where $\tilde{O}_{3D}^p$ is the 3D Fourier transform of O^p and $\hat{\mathbf{r}}(r_3')$ is the scattering direction corresponding to a point along the receiver at height r_3'. Equation (5) can further be simplified by observing that the radius of the array r is much larger than Δ, therefore $k\hat{\mathbf{r}}(r_3') \approx k\hat{\mathbf{r}}_\parallel + kr_3'/r\hat{\mathbf{r}}_\perp$, with $\hat{\mathbf{r}}_\parallel$ being the unit vector
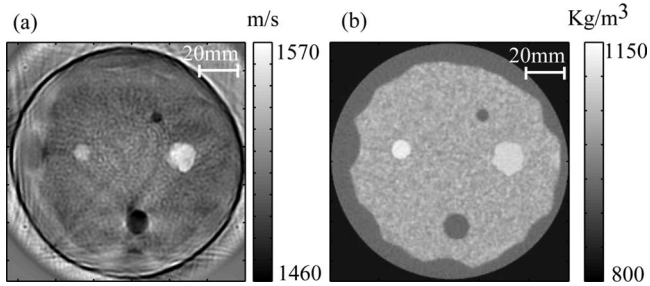
FIG. 3. Images of the cross section of the phantom containing the four inclusions. (a) Sound-speed map. (b) X-ray CT image providing the density distribution across the same slice as in (a).

in the plane of the array pointing at the receiver. By using the variable transformation $k_3 = kr_3'/r$ in Eq. (5) one obtains

$$\int_{-\Delta}^{\Delta} dr_3' \psi^p = \frac{\exp(ikr)}{4\pi k} \widetilde{O}_{2D}^p[k(\hat{\mathbf{r}}_{\parallel} - \hat{\mathbf{r}}_0)], \tag{6}$$

where $\widetilde{O}_{2D}^p$ is the 2D Fourier transform of O^p calculated in the plane of the array ($r_3' = 0$). Equation (6) is formally equivalent to conventional 2D diffraction tomography,[6,9] which is based on a proportionality relationship between the scattered field, $\psi^p - \psi_0$, and the Fourier transform of O^t, i.e., $\psi^p - \psi_0 \propto \widetilde{O}_{2D}^t[k(\hat{\mathbf{r}}_{\parallel} - \hat{\mathbf{r}}_0)]$. This expression can be derived from Eq. (2) (adjusted for the 2D case) by applying the Born approximation. However, if this expression were applied to the case considered in this letter, O^t would not be reconstructed because due to the beam deflection phenomenon, $\psi^p - \psi_0 \approx -\psi_0$ since $\psi^p \ll \psi_0$ meaning that the information about O^p is lost in the incident field.

The multiscale approach described by Eq. (6) is demonstrated by means of an experiment performed with a breast phantom tested with a 256 element ultrasonic array developed at Karmanos Cancer Institute.[4] The internal diameter of the ring is 200 mm and each element has a 0.5 mm width and 12 mm height ($2\Delta = 12$ mm). The phantom has a shape that approximate that of a truncated cone 100 mm height with 100 mm average diameter and 40° aperture. It consists of several materials mimicking a subcutaneous fat layer that embeds an irregular glandular parenchyma where the main biological functions of the breast take place, and four 3D inclusions corresponding to two tumors and two fat spheres [a diagrammatic cross section of the phantom is shown in Fig. 1(a), see also Ref. 4]. Both the array and the phantom are immersed in a water bath at 24 °C that provides the background medium. The measurements were obtained at 700 kHz which corresponds to $\lambda = 2.14$ mm in water.

Figure 2(a) shows the amplitude of the total field measured without the phantom as a function of the illumination angle, θ, and the scattering angle, ϕ, at 700 kHz. The diagonal $\theta = \phi$ refers to measurements performed with the receiver facing the transmitter, these measurements are referred to as direct transmissions. Since the wave field excited by each transducer is directional, the direct transmissions have the largest amplitudes. Next, Fig. 2(b) shows the field measured when the phantom is immersed in the water background and the plane of the array does not intersect the inclusions. Due to the curved shape of the phantom and the water-phantom impedance contrast, a strong beam deflection occurs and the direct transmission is no longer the strongest signal. Instead, the largest signals are measured for those

transmit-receive pairs joined by a ray that is tangent to the boundary of the phantom in the plane of the array. The structure of the measurements is different when the plane of the array intersects the four inclusions as shown in Fig. 2(c). In this case, in addition to the signals corresponding to the boundaries of the phantom, a number of patterns emerges close to the direct transmission measurements. These are the acoustic signatures of the four inclusions, as can be deduced from Fig. 2(d) that provides those particular transmit-receive combinations for which the straight ray from the transmitter to the receiver intersects the center of one inclusion. Therefore, thanks to the deflection caused by the body of the phantom, the field detected by the array is largely due to the energy scattered by the structures in the plane of the array (O^p) and marginally affected by the out-of-plane structures.

The measurements shown in Fig. 2(c) correspond to the LHS term in Eq. (6) and can be used to reconstruct O^p by inverting the mapping in Eq. (6) using the technique in[10] and lead to the image shown in Fig. 3(a). Indeed, the inversion uses a subset of the measurements in Fig. 2(c) that corresponds to the so-called transmission data that is used in TTT and covers a 120° interval around the diagonal $\theta = \phi$ in Fig. 2(c), i.e., $\theta - 60° < \phi < \theta + 60° \;\forall\, \theta \in [-180°, 180°]$.

To better appreciate the features of Fig. 3(a), a x-ray CT image of the same phantom obtained with a commercial scanner is shown in Fig. 3(b). Despite the fact that the CT image is a density map, there are striking similarities with the sound-speed image. Not only is the overall size of the inclusions correctly determined, but also the details of their shapes are well defined. A careful analysis of Fig. 3(a) also reveals the irregular outline of the glandular tissue. The artifact outside the phantom boundary is due to aliasing caused by the limited number of array elements which also is the reason why the subcutaneous fat is not as clearly visible as the inclusions (for a phantom diameter of 120 mm and $\lambda = 2$ mm the Nyquist criterion requires a minimum number of 377 sensors while the array has 256 only). Overall Fig. 3 demonstrates that the inversion based on the model provided by Eq. (6) achieves unprecedented tomographic image quality comparable to that obtained with x-ray CT. The time required to collect the data used to build the image in Fig. 3(a), is under 0.1 s, making the technology viable for a number of clinical applications including breast imaging.

[1] P. L. Carson, C. R. Meyer, A. L. Scherzinger, and T. V. Oughton, Science **214**, 1141 (1981).
[2] F. Pfeiffer, T. Weitkamp, O. Bunk, and C. David, Nat. Phys. **2**, 258 (2006).
[3] F. Simonetti, L. Huang, and N. Duric, J. Appl. Phys. **101**, 083103 (2007).
[4] N. Duric, L. Littrup, P. Poulo, A. Babkin, R. Pevzner, E. Holsapple, O. Rama, and C. Glide, Med. Phys. **34**, 773 (2007).
[5] J. G. Berryman, Phys. Rev. Lett. **62**, 2953 (1989).
[6] M. Born and E. Wolf, *Principles of Optics* (Cambridge University Press, Cambridge, 1999).
[7] A. C. Kak and M. Slaney, *Principles of Computerized Tomographic Reconstruction* (IEEE, New York, 1998).
[8] S. Huang and D. E. Ingber, Cancer Cells **8**, 175 (2005).
[9] E. Wolf, Opt. Commun. **1**, 153 (1969).
[10] F. Simonetti and L. Huang, J. Appl. Phys. **103**, 103110 (2008).